

Research Article

Open Access



Topochemical synthesis and structural characteristics of orientation-controlled $(\text{Bi}_{0.5}\text{Na}_{0.5})_{0.94}\text{Ba}_{0.06}\text{TiO}_3$ perovskite microplatelets

Yaqing Ma¹, Hang Xie¹, Yuan Sun¹, Qiangwei Kou¹, Linjing Liu¹, Bin Yang¹, Wenwu Cao^{1,2}, Yunfei Chang¹, Fei Li³

¹Functional Materials and Acousto-Optic Instruments Institute, Harbin Institute of Technology, Harbin 150080, Heilongjiang, China.

²Materials Research Institute and Department of Mathematics, The Pennsylvania State University, University Park, PA 16802, USA.

³Electronic Materials Research Laboratory (Key Lab of Education Ministry), State Key Laboratory for Mechanical Behavior of Materials and School of Electronic Science and Engineering, Xi'an Jiaotong University, Xi'an 710049, Shaanxi, China.

Correspondence to: Prof. Yunfei Chang, Functional Materials and Acousto-Optic Instruments Institute, Harbin Institute of Technology, Yikuang Street 2#, Harbin 150080, Heilongjiang, China. E-mail: changyunfei@hit.edu.cn

How to cite this article: Ma Y, Xie H, Sun Y, Kou Q, Liu L, Yang B, Cao W, Chang Y, Li F. Topochemical synthesis and structural characteristics of orientation-controlled $(\text{Bi}_{0.5}\text{Na}_{0.5})_{0.94}\text{Ba}_{0.06}\text{TiO}_3$ perovskite microplatelets. *Microstructures* 2022;2:2022006. <https://dx.doi.org/10.20517/microstructures.2021.13>

Received: 13 Dec 2021 **First Decision:** 10 Jan 2022 **Revised:** 24 Jan 2022 **Accepted:** 29 Jan 2022 **Published:** 16 Feb 2022

Academic Editors: Shujun Zhang, Jun Chen **Copy Editor:** Xi-Jun Chen **Production Editor:** Xi-Jun Chen

Abstract

Two-dimensional perovskite microcrystals have important applications in various electronic and energy devices. In this work, $0.94(\text{Bi}_{0.5}\text{Na}_{0.5})\text{TiO}_3$ - 0.06BaTiO_3 (0.94BNT-0.06BT) microplatelets with a pure perovskite structure, ($h00$) orientation, good crystallinity and remarkable electromechanical strain are fabricated through topochemical microcrystal conversion from Aurivillius-structured $\text{Bi}_{4.5}\text{Na}_{0.5}\text{Ti}_4\text{O}_{15}$ precursors. The formation process of the $\text{Bi}_{4.5}\text{Na}_{0.5}\text{Ti}_4\text{O}_{15}$ precursors and the topochemical conversion mechanism of the 0.94BNT-0.06BT target are systematically studied. Intermediate phases, such as $\text{Bi}_4\text{Ti}_3\text{O}_{12}$ and $\text{Bi}_{8.5}\text{Na}_{0.5}\text{Ti}_7\text{O}_{27}$, appear before the formation of pure $\text{Bi}_{4.5}\text{Na}_{0.5}\text{Ti}_4\text{O}_{15}$ at 950 °C in a NaCl molten salt. For the topochemical microcrystal conversion process, although the Aurivillius to perovskite structural transformation is completed at 900 °C, the original single-crystal precursor platelets are replaced by polycrystalline aggregates because of extensive exfoliation and disintegration events. Such microstructural damage is healed by recrystallization via Ostwald ripening through further heating to produce single-crystal 0.94BNT-0.06BT microplatelets with flat surfaces, regular shapes and homogenous distributions of Bi, Na, Ba, Ti and O at 1150 °C. Both labyrinth and stripe-like domains can be detected from these microplatelets, suggesting the coexistence of both rhombohedral and tetragonal phases, in agreement with the X-



© The Author(s) 2022. **Open Access** This article is licensed under a Creative Commons Attribution 4.0 International License (<https://creativecommons.org/licenses/by/4.0/>), which permits unrestricted use, sharing, adaptation, distribution and reproduction in any medium or format, for any purpose, even commercially, as long as you give appropriate credit to the original author(s) and the source, provide a link to the Creative Commons license, and indicate if changes were made.



ray diffraction analysis. Furthermore, local electromechanical strain with an amplitude of ~600 pm (at 10 V) is observed from the platelets along the $\langle 001 \rangle_c$ direction.

Keywords: Topochemical conversion, $(\text{Bi}_{0.5}\text{Na}_{0.5})\text{TiO}_3$ - BaTiO_3 , microstructure, piezoelectricity

INTRODUCTION

Perovskite materials with two-dimensional microstructures have attracted significant attention in recent years because of their unique shape-dependent functional properties. Anisotropic perovskite particles can be widely used as templates to texture electronic ceramics^[1-3], substrates to grow crystals or deposit films^[4,5], fillers in polymer systems for energy storage applications^[6,7] and building blocks to fabricate functional micro/nanodevices (e.g., energy harvesting systems and field effect transistors)^[8,9]. Appropriate crystal orientation, morphology and crystallinity of the particles are essential for the design of microplatelets with the desired functionality. However, anisotropic perovskite platelets are difficult to synthesize via conventional methods due to the similar surface energies of the crystal planes^[10]. Until now, the most effective method for fabricating platelet perovskites has been based on the topochemical microcrystal conversion (TMC) of two-dimensional precursors with perovskite units via the deletion, insertion or exchange of individual atoms to transform localized structures^[11-14].

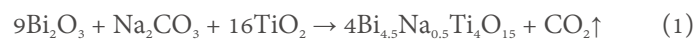
$(\text{Bi}_{0.5}\text{Na}_{0.5})\text{TiO}_3$ is considered one of the key lead-free candidates to potentially replace commercialized toxic $\text{Pb}(\text{Zr},\text{Ti})\text{O}_3$ -based systems, owing to the outstanding electrical properties of its solid solutions with other perovskite components at the morphotropic phase boundary (MPB). $(1-x)(\text{Bi}_{0.5}\text{Na}_{0.5})\text{TiO}_3$ - $x\text{BaTiO}_3$ (BNT-BT) solid solutions have recently received increasing interest, owing to their substantially enhanced piezoelectric properties achieved near the MPB (i.e., $0.05 \leq x \leq 0.07$)^[15,16]. Kang *et al.*^[17] investigated the effects of BT amount on the piezoelectric and energy harvesting properties of $(1-x)\text{BNT}$ - $x\text{BT}$ ceramics and found that the maximum piezoelectric charge coefficient $d_{33} \sim 164$ pC/N and output voltage $V \sim 8.95$ V were achieved at $x = 0.06$. Zhao *et al.*^[18] studied the polar domain structural evolution of 0.94BNT-0.06BT under external fields, while Das Adhikary *et al.*^[19] investigated its random lattice strain and relaxation, with both studies revealing the impact of these effects on the structural and electrical properties of the material. Furthermore, textured ceramics of 0.94BNT-0.06BT or similar compositions have been synthesized through templated grain growth via the use of $\text{Bi}_4\text{Ti}_3\text{O}_{12}$ ^[20], SrTiO_3 ^[21], BaTiO_3 ^[22], BNT ^[23,24] and NaNbO_3 ^[25] platelet templates. It was found that the addition of heterogeneous templates causes both lattice mismatch with the matrix and compositional changes in the final ceramics, which can deteriorate the piezoelectric properties, lower the depolarization temperature and thereby cause instability in the final textured ceramics. The utilization of BNT-BT platelets as templates instead of the above mentioned compositions could be advantageous to texture BNT-BT-based ceramics, with the aim of achieving significantly enhanced piezoelectric properties without lowering the depolarization temperature.

In this work, 0.94BNT-0.06BT microplatelets with controlled morphology and good crystallinity are fabricated by a TMC approach using Aurivillius $\text{Bi}_{4.5}\text{Na}_{0.5}\text{Ti}_4\text{O}_{15}$ (BINT) precursors. The BINT microplatelets are made of a bismuth layer-structured ferroelectric^[26] and thus can be directly fabricated by molten salt synthesis. Because success in fabricating anisotropic perovskites with controlled characteristics is an important milestone in achieving their maximum functional performance, processes on both the synthesis of the BINT precursors and their topochemical conversion into 0.94BNT-0.06BT target deserve particular attention. Therefore, the main objective of this work is to fundamentally understand the formation mechanism of 0.94BNT-0.06BT microplatelets by systematically studying their compositional/structural evolution and morphological development. Furthermore, the functionality of individual 0.94BNT-0.06BT

microplatelets is examined by studying their domain morphology and local functional response. The synthesis of high-quality BNT-BT anisotropic particles has the potential to enhance their performance in advanced applications and the investigation of their formation mechanism provides guidelines for the further design and synthesis of novel anisotropic perovskite crystals.

MATERIALS AND METHODS

Aurivillius BINT plate-like precursors were synthesized by molten salt synthesis. Reagent-grade Bi_2O_3 , Na_2CO_3 and TiO_2 powders of 99.9% purity were mixed following the stoichiometry of Equation (1) by ball-milling in ethanol for 12 h, with NaCl then added in a weight ratio of 15:1 by ball-milling for another 12 h. To study the formation process of BINT, the dried powder mixtures were heated at temperatures between 650 and 1050 °C for 1.5 h, followed by removal of the salt by washing with hot deionized water more than 15 times until no Cl⁻ was detected by the AgNO_3 solution. Next, using the BINT particles fabricated at 1050 °C as precursors, topochemical conversion of the 0.94BNT-0.06BT microplatelets was carried out according to Equation (2). Stoichiometric amounts of BINT, Na_2CO_3 , BaCO_3 and TiO_2 were mixed with NaCl in a weight ratio of 1:2. To preserve the platelet morphology of the BINT precursors, Na_2CO_3 , BaCO_3 , TiO_2 and NaCl were firstly mixed by ball-milling for 12 h and then the precursors were added by magnetic stirring for 12 h. The dried powder mixtures were heated at temperatures between 900 and 1150 °C for 6 h to study the TMC process for 0.94BNT-0.06BT. Repeated washing using hot deionized water and filtration was performed to remove the NaCl, after which the synthesized microplatelets were dispersed by ultrasonication and rinsed five times with deionized water.



X-ray diffraction (XRD, D/max 2400, Rigaku, Tokyo, Japan) was utilized to determine the phase structure and crystal orientation of the samples. Raman scattering spectra were collected through a LabRAM XploRA spectrometer (HORIBA Jobin Yvon S.A.S., France). Field-emission scanning electron microscopy (Helios Nanolab 600i, FEI, Hillsboro, OR, USA) combined with energy-dispersive X-ray spectroscopy (EDS) was utilized to observe the morphological and compositional features. Piezoelectric force microscopy (PFM, MFP-3D, Asylum Research, CA, USA) was utilized to obtain the height/amplitude/phase images and local electrical responses (phase-voltage hysteresis loop and amplitude-voltage butterfly curve) of the synthesized BNT-BT microplatelets.

RESULTS AND DISCUSSION

Figure 1 shows the phase formation sequence of the BINT precursors during the molten salt synthesis as a function of heat treatment. Below the melting point of NaCl ($T_m \sim 801$ °C), solid-state reactions had already taken place between the Bi_2O_3 , Na_2CO_3 and TiO_2 raw materials at 650 °C, so the peaks for the $\text{Bi}_4\text{Ti}_3\text{O}_{12}$ (JCPDS card #80-2143) and BNT (JCPDS card #89-3109) intermediate phases can be clearly detected from the XRD pattern. With increasing temperature to 805 °C, the NaCl melted and the Aurivillius-structured BINT (JCPDS card #74-1316) phase began to form. Furthermore, the $\text{Bi}_{8.5}\text{Na}_{0.5}\text{Ti}_7\text{O}_{27}$ (JCPDS card #32-1044) intermediate phase, consisting of structural units of the two parent phases, $\text{Bi}_4\text{Ti}_3\text{O}_{12}$ ($m = 3$) and BINT ($m = 4$), through sharing of the “ Bi_2O_2 ” sheets along the c -axis^[27], was detected. The $\text{Bi}_{8.5}\text{Na}_{0.5}\text{Ti}_7\text{O}_{27}$ peak intensities increase with increasing temperature to 825 °C and then decrease at 850 °C. Finally, all intermediate phases were consumed and completely converted into the pure BINT phase at 950 °C, which remained stable with a further increase temperature to 1050 °C.

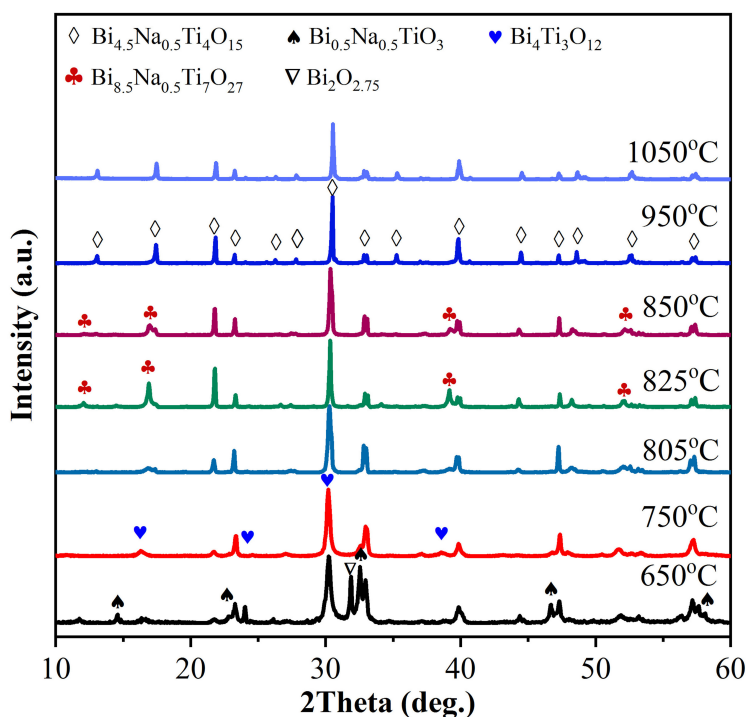


Figure 1. Phase formation of BINT precursors during molten salt synthesis process.

Figure 2 demonstrates the morphology formation for the BINT precursors during the molten salt synthesis. Relatively agglomerate platelet particles with side lengths of ~ 0.4 - $2.4 \mu\text{m}$ can be detected in the molten salt at 805°C , which can be attributed to the mixture of $\text{Bi}_4\text{Ti}_3\text{O}_{12}$, $\text{Bi}_{8.5}\text{Na}_{0.5}\text{Ti}_7\text{O}_{27}$ and BINT phases according to **Figure 1**. With a further increase to 900°C , the platelets become larger, well dispersed and more homogeneous, with side lengths of ~ 1.1 - $3.7 \mu\text{m}$ detected. Discrete and well-oriented platelet particles with side lengths of ~ 2.6 - $7.4 \mu\text{m}$ and thicknesses of ~ 0.2 - $0.3 \mu\text{m}$ were obtained at 950°C , which were confirmed to be of the pure Aurivillius BINT phase in **Figure 1**. These anisotropic BINT platelets possess a structure expressed by the general formula $\text{Bi}_2\text{O}_2(\text{A}_{m-1}\text{B}_m\text{O}_{3m+1})$, where A represents the mixture of Na^+ and Bi^{3+} (perovskite A-site with twelvefold coordination), B represents Ti^{4+} (perovskite B-site with sixfold coordination) and $m = 4$, which means that the structure of BINT consists of four perovskite-like $[(\text{Bi}_{2.5}\text{Na}_{0.5})\text{Ti}_4\text{O}_{13}]^{2+}$ layers between the two $(\text{Bi}_2\text{O}_2)^{2+}$ fluorite layers. With further increasing temperature to 1050°C , the reaction proceeds into the particle growth stage [**Figure 1**], so BINT platelets with larger particle sizes (6.0 - $12.0 \mu\text{m}$ in side length and 0.3 - $0.8 \mu\text{m}$ in thickness), regular shapes and high aspect ratios were obtained, which were used as suitable precursors for the topochemical conversion of the 0.94BNT - 0.06BT perovskite target.

Figure 3A displays the XRD patterns of the product(s) obtained by heating the BINT, Na_2CO_3 , BaCO_3 and TiO_2 mixture at different temperatures. Pure perovskite phase was detected at 900°C , suggesting the completed structural conversion from the Aurivillius precursor to the perovskite target. Three possible processes could finish at this temperature. The first is that $(\text{Bi}_2\text{O}_2)^{2+}$ interlayers reacted with ambient O^{2-} and then decomposed from the BINT crystal lattice in the form of Bi_2O_3 , owing to the weak linkage between $(\text{Bi}_2\text{O}_2)^{2+}$ layers and $[(\text{Bi}_{2.5}\text{Na}_{0.5})\text{Ti}_4\text{O}_{13}]^{2+}$ blocks. The second one is that Na^+ and Ba^{2+} ions partially replaced the Bi^{3+} ions in the pseudo-perovskite blocks. The third one is that the byproduct Bi_2O_3 may have reacted with some Na_2CO_3 , BaCO_3 and TiO_2 to form isotropic perovskite BNT-BT particles. Further investigation is needed to clarify these complicated structural evolution processes. The formed perovskite phase maintains

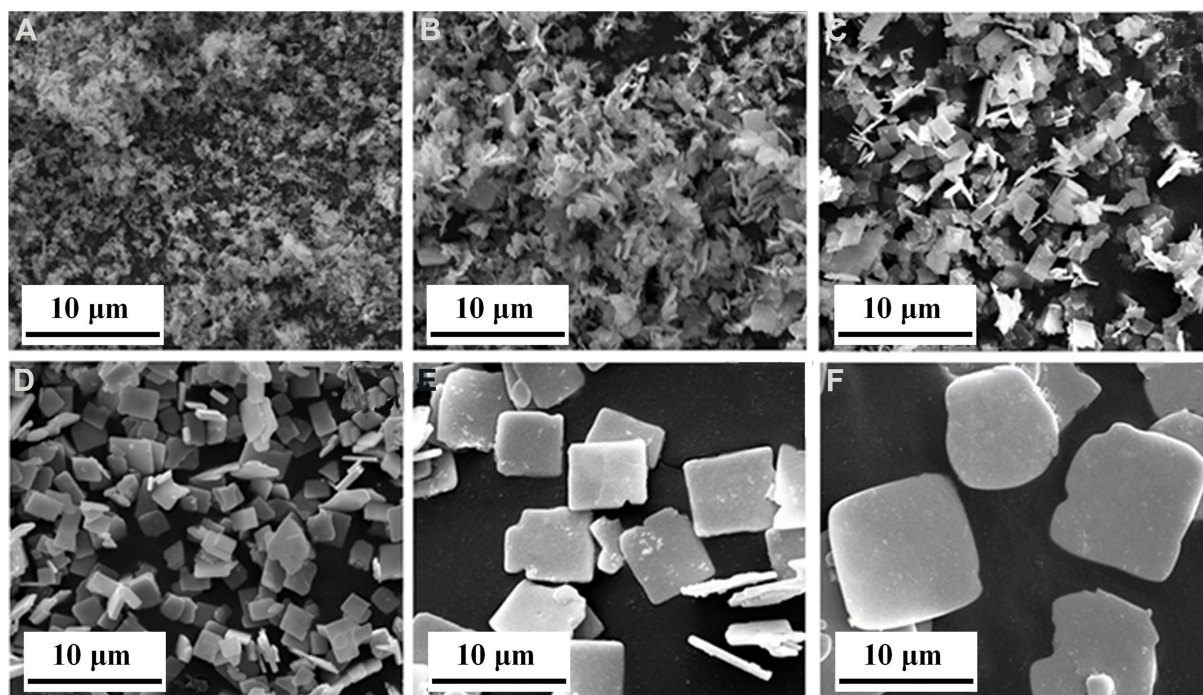


Figure 2. Morphology formation for BINT precursors during molten salt synthesis at different heating temperatures of (A) 750, (B) 805, (C) 850, (D) 900, (E) 950 and (F) 1050 °C.

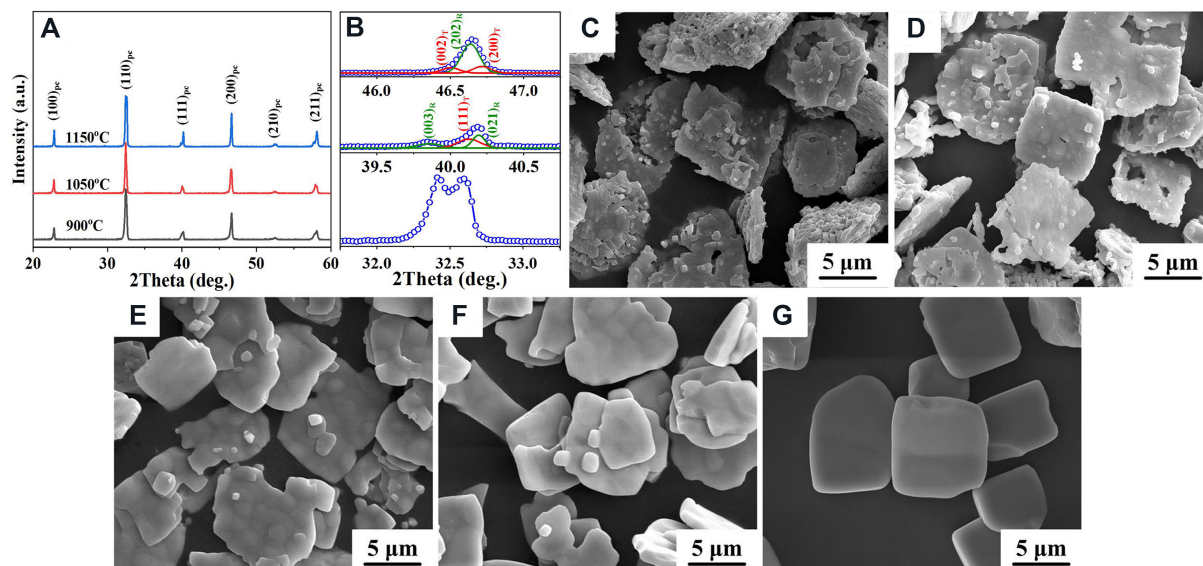


Figure 3. (A) XRD patterns of converted product(s) obtained at different heating temperatures. The diffraction peaks were indexed based on the pseudocubic unit cell (pc) because of rhombohedral distortion. (B) Details of the XRD pattern in the 2θ ranges of 32.0° - 33.0° , 39.5° - 40.5° and 46.0° - 47.0° for the product obtained at 1150 °C. The latter two peaks were fitted using the Gaussian function as examples. Morphological evolution during the Aurivillius BINT to perovskite 0.94BNT-0.06BT conversion process at different heating temperatures of (C) 900, (D) 1000, (E) 1050, (F) 1100 and (G) 1150 °C.

its stability with further increasing temperature to 1050 and 1150 °C. For the product obtained at 1150 °C, close inspection of the XRD data [Figure 3B] reveals two sets of peaks, which were fitted to a mixture of rhombohedral and tetragonal phases in space groups $R3c$ and $P4bm$, respectively, using the Gaussian

function. Such splitting of peaks in the XRD pattern suggests that the composition of the final product is in the range of the MPB, which is consistent with that reported previously for 0.94BNT-0.06BT ceramics^[28,29].

Figure 3C-G present the morphological evolution of the structurally converted perovskite particles during the heating process. Many polycrystalline aggregates, which roughly preserved the shape/size of the BINT precursors and consisted of aligned perovskite grains, could be observed at 900 °C. Such a phenomenon indicates that extensive exfoliation and disintegration events occurred during the structural transformation process from Aurivillius to perovskite phase, possibly owing to the loss of epitaxy and expulsion of the Bi₂O₃ byproduct^[13]. Furthermore, some fine isotropic perovskite particles can also be detected. These polycrystalline aggregates recrystallize with increasing heating temperature, accompanied by the disappearance of both several polycrystalline boundaries and pores inside the aggregates. The converted platelets still possessed the polycrystalline feature with rugged surfaces and irregular shapes at 1100 °C, but they became much denser. With further increasing temperature to 1150 °C, single-crystal BNT-BT microplatelets with flat surfaces, regular shapes and increased thicknesses were obtained. These platelets were ~6.1-10.5 μm in length and ~0.9-2.0 μm in thickness. The microstructure/crystallinity damage caused by the structural conversion was completely healed at this stage, which occurred through secondary recrystallization or Ostwald ripening^[30]. To be specific, the polycrystalline aggregates sintered and recrystallized into the single crystals. In addition, Ostwald ripening, i.e., the growth of larger particles by consuming smaller ones, promoted further growth and reshaping of these irregular microcrystals, producing final platelets with regular shapes and increased thickness.

Figure 4A shows the XRD patterns of the aligned BINT precursors and 0.94BNT-0.06BT platelets. The BINT precursors are of the pure Aurivillius phase (JCPDS card #74-1316). The strong intensities of the (006), (008), (0010), (0016) and (0020) peaks indicate that the surfaces of the precursor platelets were parallel to (00 l), suggesting that these particles are highly-oriented and thus good precursor candidates. The converted 0.94BNT-0.06BT microcrystals are identified to be of the pure perovskite phase (JCPDS card #89-3109). Only the (100)_{pc} and (200)_{pc} peaks can be detected from the XRD pattern, suggesting the structural compatibility between BINT (00 l) and 0.94BNT-0.06BT ($h00$). Figure 4A indicates that highly ($h00$)-oriented 0.94BNT-0.06BT platelet particles can be obtained through TMC from layer-structured BINT precursors with strong (00 l) orientation. EDS was conducted to determine the elemental distribution and composition of the converted microplatelets. The elemental distribution maps [Figure 4B] show the homogenous distributions of Bi, Na, Ba, Ti and O for the platelets. According to the EDS analysis, the actual chemical composition of the converted platelets approximately agrees with the nominal 0.94BNT-0.06BT composition of crystal growth. A schematic illustration of the topological mechanism responsible for the conversion from BINT precursors to 0.94BNT-0.06BT microplatelets is shown in Figure 5.

Raman scattering is sensitive to short-range order and phase structure, so the 0.94BNT-0.06BT microplatelets possess different Raman responses compared to the BINT precursors, as shown in Figure 4C. For bismuth layer-structured ferroelectrics, the Raman active modes are believed to originate from both A-site cations within the pseudo-perovskite blocks (below 200 cm⁻¹) and the internal vibration of the TiO₆ octahedra in the high-frequency region. Therefore, for the Aurivillius BINT, the most prominent band at ~270 cm⁻¹ could be ascribed to F_{2g} symmetry, corresponding to the interbond angle bending vibration^[31]. The bands at ~544 and ~856 cm⁻¹ are assigned to the E_g and A_{1g} characters, respectively, reflecting two pure bond stretching vibrations of the TiO₆ octahedra^[31]. For the 0.94BNT-0.06BT platelets, six vibration modes can be observed at 135, 270, 529, 561, 765 and 842 cm⁻¹, which are in good agreement with those reported in ceramics with similar compositions^[32]. These Raman bands are relatively broad and were possibly caused by the presence of the disorder structural or distorted octahedral clusters at short range and the overlapping of

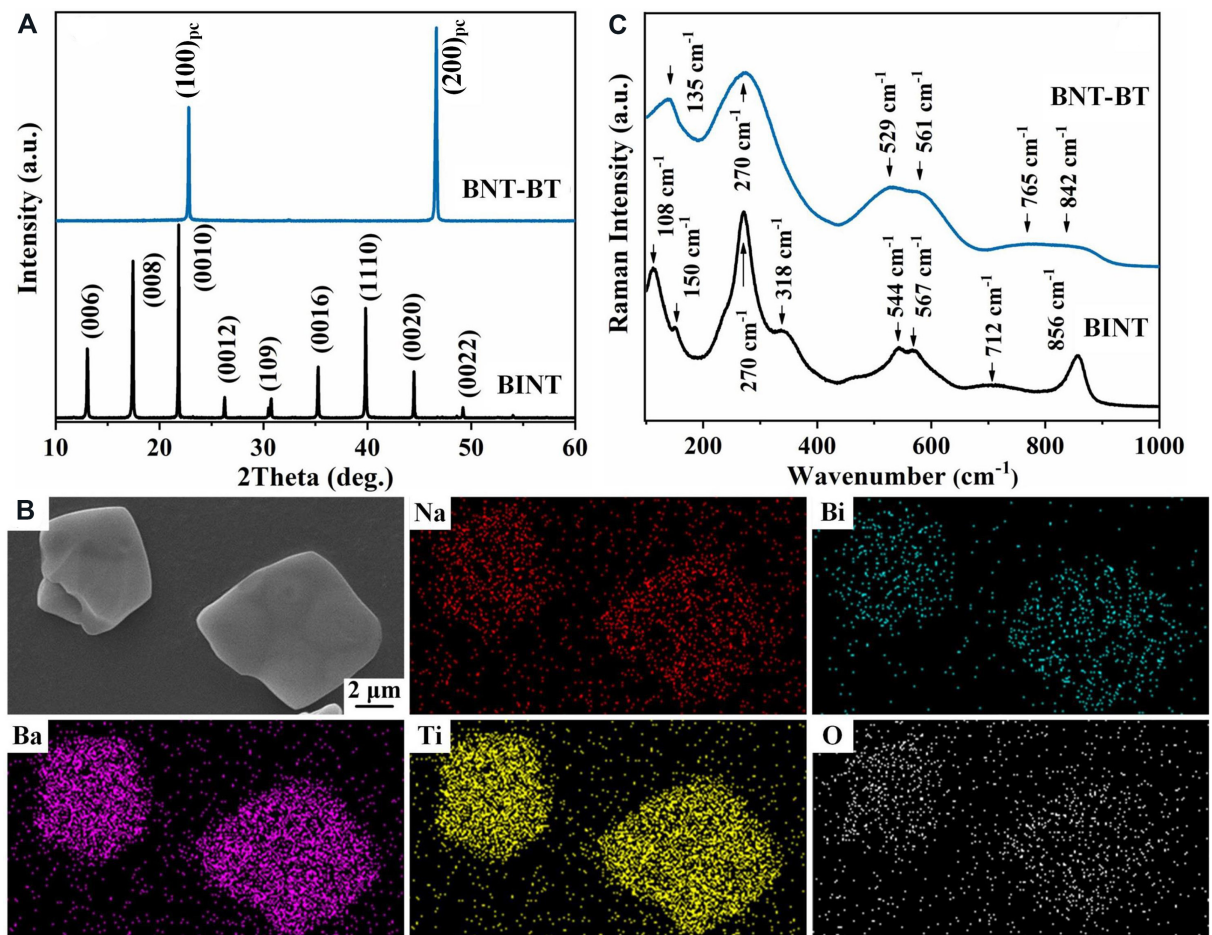


Figure 4. (A) XRD patterns of aligned Aurivillius BINT precursors and perovskite 0.94BNT-0.06BT platelets by casting them on glass substrates. (B) Elemental distribution maps of 0.94BNT-0.06BT platelets. (C) Raman spectra of BINT precursors and perovskite 0.94BNT-0.06BT platelets.

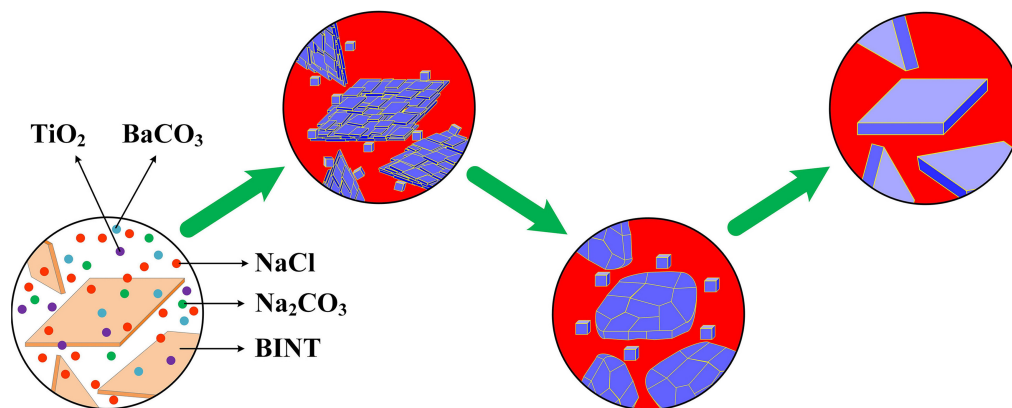


Figure 5. Schematic illustration of topological mechanism responsible for the conversion from BINT precursors to 0.94BNT-0.06BT microplatelets.

Raman modes because of the lattice anharmonicity^[33]. The Raman band near 135 cm^{-1} is correlated to the vibration of A-site ions (Na^+ , Ba^{2+} and Bi^{3+}) in the ABO_3 material, which is more sensitive to the phase

transition induced by the symmetry change in the A-site. The Raman peak at 270 cm^{-1} could be ascribed to stretching arising from the bonds owing to the presence of octahedral $[\text{TiO}_6]$ clusters at short range^[33]. The Raman bands near 529 and 561 cm^{-1} could be ascribed to the $(\leftarrow\text{O}\leftarrow\text{Ti}\rightarrow\text{O}\rightarrow)$ stretching symmetric vibrations of the octahedral $[\text{TiO}_6]$ clusters^[34]. The Raman peak at $\sim 842\text{ cm}^{-1}$ could be associated with the presence of oxygen vacancies^[29].

Figure 6A-C demonstrate the PFM height, amplitude and phase images of the 0.94BNT-0.06BT platelets converted from the BINT precursors, respectively. Relatively smooth large surfaces were also observed from the topographic PFM measurement. The phase image shows fine domains with both labyrinth and stripe shapes, suggesting the coexistence of rhombohedral and tetragonal phases in these samples. This result agrees well with the XRD patterns in Figure 3A and B. A good-symmetry phase-voltage hysteresis loop and well-shaped amplitude-voltage butterfly curve were tested at local positions of the platelets parallel to the $\langle 001 \rangle_c$ thickness direction using local switching spectroscopy PFM (SS-PFM) by applying a sequence of DC voltage from -10 to 10 V with a superimposed AC signal of 1 V to the PFM tip. A nearly 180° phase reversal was observed from phase-voltage hysteresis loop [Figure 6D], possibly indicating sufficient polarization of the sample. Furthermore, the amplitude-voltage butterfly curve [Figure 6E] demonstrates that an amplitude of surface displacement of $\sim 600\text{ pm}$ was achieved at 10 V , possibly suggesting the existence of remarkable local piezoelectricity for these microplatelets. SS-PFM can detect the electromechanical strain resulting from the converse piezoelectric effect, but such electromechanical strain on the surface can stem from several non-piezoelectric origins (i.e., artifacts), such as electrostatic interaction, charge injection, Joule heating and ion migration^[35-37].

During the testing of the phase-voltage hysteresis loop and amplitude-voltage butterfly curve shown in Figure 6D and E, respectively, we utilized a stiff cantilever and observed the off-field responses to minimize the electrostatic interaction effect^[35,37,38]. However, the possibility of contributions from artifact effects still cannot be excluded. Therefore, further studies are needed to confirm the presence of ferroelectricity and piezoelectricity in the 0.94BNT-0.06BT platelets, including writing up and down domains to prove that the measurement of the PFM signal was due to inversion of the polarization vector and not to the accumulation of charges. The orientation-controlled platelet morphology, pure perovskite structure, good crystallinity and remarkable local electromechanical strain make 0.94BNT-0.06BT platelets attractive to be used as building blocks for the fabrication of energy harvesting/storage devices, as templates to texture electronic ceramics and as substrates to grow crystals or deposit films.

CONCLUSIONS

Single-crystal $0.94(\text{Bi}_{0.5}\text{Na}_{0.5})\text{TiO}_3$ - 0.06BaTiO_3 microplatelets with preferential ($h00$) orientation, pure perovskite structure, controlled morphology and remarkable functional response were fabricated by topochemical conversion from Aurivillius $\text{Bi}_{4.5}\text{Na}_{0.5}\text{Ti}_4\text{O}_{15}$ precursors. The pure $\text{Bi}_{4.5}\text{Na}_{0.5}\text{Ti}_4\text{O}_{15}$ phase formed at $950\text{ }^\circ\text{C}$ from intermediate phases, such as $\text{Bi}_4\text{Ti}_3\text{O}_{12}$ and $\text{Bi}_{8.5}\text{Na}_{0.5}\text{Ti}_7\text{O}_{27}$, during the molten salt synthesis. The Aurivillius to perovskite structure transformation was completed at $900\text{ }^\circ\text{C}$, but the induced extensive exfoliation events led to the replacement of single-crystal platelets by polycrystalline aggregates. The subsequent recrystallization process, which occurred at higher temperatures via Ostwald ripening, healed such microstructural damage. The $0.94(\text{Bi}_{0.5}\text{Na}_{0.5})\text{TiO}_3$ - 0.06BaTiO_3 microplatelets with both single-crystal features and homogenous distributions of Bi, Na, Ba, Ti and O were achieved at $1150\text{ }^\circ\text{C}$, in which both labyrinth and stripe domains were detected, suggesting the coexistence of rhombohedral and tetragonal phases, in agreement with the XRD result. Moreover, these platelets possessed remarkable local electromechanical strain response along the $\langle 001 \rangle_c$ direction, with an amplitude of $\sim 600\text{ pm}$ detected at 10 V through SS-PFM. This work provides guidelines for the further design and synthesis of novel low-

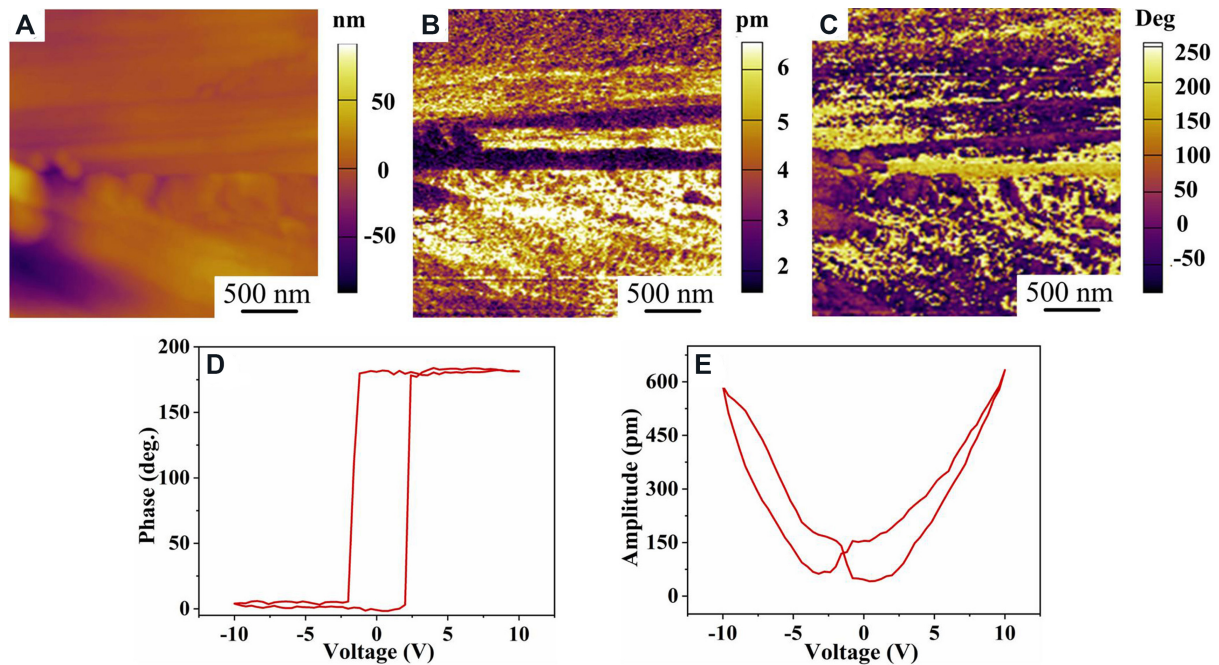


Figure 6. PFM (A) height, (B) amplitude and (C) phase images, (D) local phase-voltage hysteresis loop and (E) amplitude-voltage butterfly curve of 0.94BNT-0.06BT microplatelets converted from BINT precursors.

dimensional functional microcrystals in the future and can also remarkably expand the application fields of $(\text{Bi}_{0.5}\text{Na}_{0.5})\text{TiO}_3$ - BaTiO_3 materials.

DECLARATIONS

Authors' contributions

Conception, design, writing and editing: Ma YQ, Chang YF, Li F

Materials synthesis and structural characterizations: Ma YQ, Xie H, Liu, LJ, Kou QW, Sun Y

Data analysis and interpretation: Yang B, Cao WW, Chang YF, Li F

All authors contribute to the manuscript and were involved in discussion

Availability of data and materials

Not applicable.

Financial support and sponsorship

This work was supported by the National Natural Science Foundation of China (Nos. 52072092, 51922083 and 11572103), the Natural Science Foundation of Heilongjiang Province (No. YQ2019E026) and the Fundamental Research Funds for the Central Universities (No. HIT.OCEF.2021018).

Conflicts of interest

All authors declared that there are no conflicts of interest.

Ethical approval and consent to participate

Not applicable.

Consent for publication

Not applicable.

Copyright

© The Author(s) 2022.

REFERENCES

1. Messing GL, Trolier-mckinstry S, Sabolsky EM, et al. Templated grain growth of textured piezoelectric ceramics. *Critical Reviews in Solid State and Materials Sciences* 2004;29:45-96. DOI
2. Li J, Shen Z, Chen X, et al. Grain-orientation-engineered multilayer ceramic capacitors for energy storage applications. *Nat Mater* 2020;19:999-1005. DOI PubMed
3. Chang Y, Wu J, Liu Z, et al. Grain-oriented ferroelectric ceramics with single-crystal-like piezoelectric properties and low texture temperature. *ACS Appl Mater Interfaces* 2020;12:38415-24. DOI PubMed
4. Rehrig PW, Messing GL, Trolier-mckinstry S. Templated grain growth of barium titanate single crystals. *J Am Ceram Soc* 2000;83:2654-60. DOI PubMed
5. Chai G, Wang S, Xia Z, et al. Pbl₂ platelets for inverted planar organolead Halide Perovskite solar cells via ultrasonic spray deposition. *Semicond Sci Technol* 2017;32:074003. DOI
6. Pan ZB, Liu BH, Zhai JW, et al. NaNbO₃ two-dimensional platelets induced highly energy storage density in trilayered architecture composites. *Nano Energy* 2017;40:587-95. DOI
7. Wang L, Gao F, Xu J, et al. Enhanced dielectric tunability and energy storage properties of plate-like Ba_{0.6}Sr_{0.4}TiO₃/poly(vinylidene fluoride) composites through texture arrangement. *Compos Sci Technol* 2018;158:112-20. DOI
8. Koka A, Zhou Z, Tang H, Sodano HA. Controlled synthesis of ultra-long vertically aligned BaTiO₃ nanowire arrays for sensing and energy harvesting applications. *Nanotechnology* 2014;25:375603. DOI PubMed
9. Zhou J, Xie L, Song XF, et al. High-performance vertical field-effect transistors based on all-inorganic perovskite microplatelets. *J Mater Chem C* 2020;8:12632-7. DOI
10. Kržmanc MM, Jančar B, Uršič H, Tramšek M, Suvorov D. Tailoring the shape, size, crystal structure, and preferential growth orientation of BaTiO₃ plates synthesized through a topochemical conversion process. *Crystal Growth & Design* 2017;17:3210-20. DOI
11. Ranmohotti KG, Josepha E, Choi J, Zhang J, Wiley JB. Topochemical manipulation of perovskites: low-temperature reaction strategies for directing structure and properties. *Adv Mater* 2011;23:442-60. DOI PubMed
12. Li L, Deng J, Chen J, Xing X. Topochemical molten salt synthesis for functional perovskite compounds. *Chem Sci* 2016;7:855-65. DOI PubMed PMC
13. Poterala SF, Chang Y, Clark T, Meyer RJ, Messing GL. Mechanistic interpretation of the Aurivillius to perovskite topochemical microcrystal conversion process. *Chem Mater* 2010;22:2061-8. DOI
14. Fu J, Hou Y, Zheng M, Zhu M. Topochemical conversion of (111) BaTiO₃ piezoelectric microplatelets using Ba₆Ti₁₇O₄₀ as the precursor. *Crystal Growth & Design* 2019;19:1198-205. DOI
15. Zheng T, Wu J, Xiao D, Zhu J. Recent development in lead-free perovskite piezoelectric bulk materials. *Prog Mater Sci* 2018;98:552-624. DOI
16. Zhang S, Malič B, Li J, Rödel J. Lead-free ferroelectric materials: prospective applications. *J Mater Res* 2021;36:985-95. DOI
17. Kang W, Koh J. (1-x)Bi_{0.5}Na_{0.5}TiO₃-xBaTiO₃ lead-free piezoelectric ceramics for energy-harvesting applications. *J Eur Ceram Soc* 2015;35:2057-64. DOI
18. Zhao J, Zhang N, Ren W, et al. Polar domain structural evolution under electric field and temperature in the (Bi_{0.5}Na_{0.5})TiO₃-0.06BaTiO₃ piezoceramics. *J Am Ceram Soc* 2019;102:437-47. DOI
19. Das Adhikary G, Khatua DK, Senyshyn A, Ranjan R. Random lattice strain and its relaxation towards the morphotropic phase boundary of Na_{0.5}Bi_{0.5}TiO₃-based piezoelectrics: impact on the structural and ferroelectric properties. *Phys Rev B* 2019;99:174112. DOI
20. Kimura T, Takahashi T, Tani T, Saito Y. Crystallographic texture development in bismuth sodium titanate prepared by reactive-templated grain growth method. *J Am Ceram Soc* 2004;87:1424-9. DOI
21. Lee D, Jeong S, Park E, Song J. Characteristic of grain oriented (Bi_{0.5}Na_{0.5})TiO₃-BaTiO₃ ceramics. *J Electroceram* 2006;17:505-8. DOI
22. Su S, Zuo R. Fabrication and electrical properties of 0.94Na_{0.5}Bi_{0.5}TiO₃-0.06BaTiO₃ textured ceramics by RTGG method using micrometer sized BaTiO₃ plate-like templates. *J Alloys Compd* 2012;525:133-6. DOI
23. Maurya D, Zhou Y, Yan Y, Priya S. Synthesis mechanism of grain-oriented lead-free piezoelectric Na_{0.5}Bi_{0.5}TiO₃-BaTiO₃ ceramics with giant piezoelectric response. *J Mater Chem C* 2013;1:2102. DOI
24. Ma S, Zhang Y, Liu Z, et al. Preparation and enhanced electric-field-induced strain of textured 91BNT-6BT-3KNN lead-free piezoceramics by TGG method. *J Mater Sci: Mater Electron* 2016;27:3076-81. DOI
25. Bai W, Wang L, Zheng P, Wen F, Zhai J, Ji Z. Pairing high piezoelectric properties and enhanced thermal stability in grain-oriented BNT-based lead-free piezoceramics. *Ceramics International* 2018;44:11402-9. DOI
26. Zhao W, Zhou H, Yan Y, Liu D. Topochemical synthesis of plate-like Na_{0.5}Bi_{0.5}TiO₃ from Aurivillius precursor. *J American Ceramic*

- Society* 2008;91:1322-5. DOI
27. Yokoi A, Sugishita J. Ferroelectric properties of mixed bismuth layer-structured $\text{Na}_{0.5}\text{Bi}_{8.5}\text{Ti}_7\text{O}_{27}$ ceramic and $\text{Sr}_x\text{Na}_{0.5-x}/2\text{Bi}_{8.5-x/2}\text{Ti}_7\text{O}_{27}$ solid solutions. *J Alloys Compd* 2008;452:467-72. DOI
 28. Chen M, Xu Q, Kim BH, et al. Structure and electrical properties of $(\text{Na}_{0.5}\text{Bi}_{0.5})_{1-x}\text{Ba}_x\text{TiO}_3$ piezoelectric ceramics. *J Eur Ceram Soc* 2008;28:843-9. DOI
 29. Prado-espinoza A, Camargo J, del Campo A, Rubio-marcos F, Castro M, Ramajo L. Exploring new methodologies for the identification of the morphotropic phase boundary region in the $(\text{BiNa})\text{TiO}_3$ - BaTiO_3 lead free piezoceramics: Confocal Raman Microscopy. *J Alloys Compd* 2018;739:799-805. DOI
 30. Rahaman MN. Ceramic processing and sintering. 2nd ed. New York: CRC Press; 2003. p. 546-53.
 31. Jiang X, Jiang X, Chen C, et al. Photoluminescence, structural, and electrical properties of erbium-doped $\text{Na}_{0.5}\text{Bi}_{4.5}\text{Ti}_4\text{O}_{15}$ ferroelectric ceramics. *J Am Ceram Soc* 2016;99:1332-9. DOI
 32. Zhao J, Zhang N, Quan Y, et al. Evolution of mesoscopic domain structure and macroscopic properties in lead-free $\text{Bi}_{0.5}\text{Na}_{0.5}\text{TiO}_3$ - BaTiO_3 ferroelectric ceramics. *J Appl Phys* 2021;129:084103. DOI
 33. Badapanda T, Sahoo S, Nayak P. Dielectric, ferroelectric and piezoelectric study of BNT-BT solid solutions around the MPB region. *IOP Conf Ser: Mater Sci Eng* 2017;178:012032. DOI
 34. Parija B, Badapanda T, Panigrahi S, Sinha TP. Ferroelectric and piezoelectric properties of $(1-x)(\text{Bi}_{0.5}\text{Na}_{0.5})\text{TiO}_3$ - BaTiO_3 ceramics. *J Mater Sci: Mater Electron* 2013;24:402-10. DOI
 35. Flores-ruiz F, Gervacio-Arciniega J, Murillo-Bracamontes E, Cruz M, Yáñez-Limón J, Siqueiros J. An alternative scheme to measure single-point hysteresis loops using piezoresponse force microscopy. *Measurement* 2017;108:143-51. DOI
 36. Balke N, Jesse S, Li Q, et al. Current and surface charge modified hysteresis loops in ferroelectric thin films. *J Appl Phys* 2015;118:072013. DOI
 37. Miller A, Carchman R, Long R, Denslow SA. La Crosse viral infection in hospitalized pediatric patients in Western North Carolina. *Hosp Pediatr* 2012;2:235-42. DOI PubMed
 38. Hong S, Woo J, Shin H, et al. Principle of ferroelectric domain imaging using atomic force microscope. *J Appl Phys* 2001;89:1377-86. DOI